in MT (minus end) focusing at the cell center. These included lack of fusion of MT overlap regions and features indicative of MT minus-end localization at the cell periphery, such as MT growth from the cell end inward and MT depolymerization ("shrinkage") all the way to the cell tip (Fig. 3F). *klp2*Δ cells also displayed decreased IMA stability. Although the frequencies of IMA nucleation and fusion in *klp2*Δ cells were similar to those in the wild type, the frequency of IMA "separation" and catastrophe was increased by a factor of 3 in *klp2*Δ cells (0.20 events/min and 0.26 events/min, respectively; Fig. 4A) (table S1). In addition, IMAs in *klp2*Δ and wild-type cells were unstable in the presence of the MT-depolymerizing drug carbendazim (MBC) but, unlike in control cells, the number of MBC-stable MT remnants in *klp2*Δ cells decreased with time of exposure to the drug (Fig. 4B), and IMAs reassembled after drug removal frequently failed to occupy the whole cell length (Fig. 4C).

To determine whether Klp2 was involved in the generation of uniformly polarized MTs, we examined the movement of the GFP-labeled cell end marker Tea1 in wild-type and *klp2*Δ cells. Tea1 particles associate with MT plus ends and travel outward from the cell center (*1*, *14*, *18*), and so act as a marker of MT polarization. In kymographs of wild-type cells, 90% of Tea1-GFP moved outward and 10% inward (231 particles, 25 cells; Fig. 4D), indicating a factor of 9 excess of MT plus-end orientation toward the cell tips. In *klp2*Δ cells, the corresponding values were 75% outward and 25% inward (310 particles, 24 cells; Fig. 4D), indicating only a factor of 3 excess of MT plus-end orientation toward the cell tips. This difference was enhanced in elongated cells generated by treatment for 5 hours with the DNA synthesis inhibitor hydroxyurea (HU). In HU-treated wild-type cells, 71% of Tea1-GFP moved outward and 29% inward (565 particles, 29 cells; Fig. 4E and movie S7), whereas in HU-treated *klp2*Δ cells the values were 57% outward and 43% inward (695 particles; 29 cells; Fig. 4E and movie S8). These indicate, respectively, a factor of 2.5 and a factor of 1.3 excess of MT plus-end orientation toward the cell tips. A value of 1.3 is close to random (i.e., 50% outward and 50% inward), indicating that in elongated cells Klp2 is required to maintain normal MT polarization with MT plus ends oriented toward the cell tips.

Klp2 is a member of the conserved Kar3/Ncd family of minus end–directed KLPs (*19*) that generally act in mitotic and meiotic spindles. Its *Drosophila melanogaster* homolog Ncd exerts an inward force on spindle poles by cross-linking and sliding interpolar MTs (*20*), and moves along MTs at ~16 μm/min in vitro (*21*). In the fission yeast, Klp2 regulates spindle size (*17*) and localizes to MTs during interphase (*17*). We suggest that, like bipolar spindles (*22*–*27*), fission yeast interphase MTs require motor activity for their proper organization. We propose that Klp2 mediates minus end–directed sliding of cytoplasmic MTs relative to each other, which is necessary to maintain the uniform polarization of interphase microtubular arrays (fig. S3). Interestingly, interphase microtubule organizing center integrity can be lost upon disruption of minus-ended motor complexes in mammalian cells (*28*). Hence, minus end–directed MT sliding may contribute to interphase MT polarization in other eukaryotes.

References and Notes

1. J. Mata, P. Nurse, *Cell* **89**, 939 (1997).
2. J. Hayles, P. Nurse, *Nat. Rev. Mol. Cell Biol.* **2**, 647 (2001).
3. D. R. Drummond, R. A. Cross, *Curr. Biol.* **10**, 766 (2000).
4. P. T. Tran, L. Marsh, V. Doye, S. Inoue, F. Chang, *J. Cell Biol.* **153**, 397 (2001).
5. M. J. Sagolla, S. Uzawa, W. Z. Cande, *J. Cell Sci.* **116**, 4891 (2003).
6. R. Ding, R. R. West, D. M. Morphew, B. R. Oakley, J. R. McIntosh, *Mol. Biol. Cell* **8**, 1461 (1997).
7. D. Brunner, P. Nurse, *Cell* **102**, 695 (2000).
8. K. E. Sawin, P. C. Lourenco, H. A. Snaith, *Curr. Biol.* **14**, 763 (2004).
9. A. Yamamoto, R. R. West, J. R. McIntosh, Y. Hiraoka, *J. Cell Biol.* **145**, 1233 (1999).
10. See supporting data on *Science* Online.
11. S. R. Heidemann, *Methods Enzymol.* **196**, 469 (1991).
12. V. I. Rodionov, G. G. Borisy, *Science* **275**, 215 (1997).
13. S. C. Brazer, H. P. Williams, T. G. Chappell, W. Z. Cande, *Yeast* **16**, 149 (2000).
14. H. Browning, D. D. Hackney, P. Nurse, *Nat. Cell Biol.* **5**, 812 (2003).
15. R. R. West, T. Malmstrom, C. L. Troxell, J. R. McIntosh, *Mol. Biol. Cell* **12**, 3919 (2001).
16. J. L. Paluh *et al.*, *Mol. Biol. Cell* **11**, 1225 (2000).
17. C. L. Troxell *et al.*, *Mol. Biol. Cell* **12**, 3476 (2001).
18. R. Behrens, P. Nurse, *J. Cell Biol.* **157**, 783 (2002).
19. S. A. Endow, *Eur. J. Biochem.* **262**, 12 (1999).
20. D. J. Sharp, K. R. Yu, J. C. Sisson, W. Sullivan, J. M. Scholey, *Nat. Cell Biol.* **1**, 51 (1999).
21. S. A. Endow, H. Higuchi, *Nature* **406**, 913 (2000).
22. A. Dammermann, A. Desai, K. Oegema, *Curr. Biol.* **13**, R614 (2003).
23. U. S. Tulu, N. M. Rusan, P. Wadsworth, *Curr. Biol.* **13**, 1894 (2003).
24. N. M. Rusan, U. S. Tulu, C. Fagerstrom, P. Wadsworth, *J. Cell Biol.* **158**, 997 (2002).
25. T. Wittmann, A. Hyman, A. Desai, *Nat. Cell Biol.* **3**, E28 (2001).
26. T. J. Keating, G. G. Borisy, *Biol. Cell.* **91**, 321 (1999).
27. A. Hyman, E. Karsenti, *J. Cell Sci.* **111**, 2077 (1998).
28. N. J. Quintyne *et al.*, *J. Cell Biol.* **147**, 321 (1999).

29. K. E. Busch, D. Brunner, *Curr. Biol.* **14**, 548 (2004).
30. We thank E. Piddini, M. Godinho-Ferreira, H. Masuda, U. Euteneuer, T. Toda, F. Uhlmann, N. Hirokawa, T. Wittmann, J. Höög, F. Chang, J. R. McIntosh, and members of the Nurse lab for discussions; E. Karsenti, J. R. McIntosh, K. Sawin, and D. Brunner for materials; and E. Piddini, F. Uhlmann, J. Hayles, M. Pardo, S. Castagnetti, J. Zhurinsky, J. R. McIntosh, M. Godinho-Ferreira, and T. Surrey for reading the manuscript. Supported by an International Human Frontier Science Program Organization (HFSPO) postdoctoral fellowship (R.E.C.-S.), HFSPO (ST00069/2001-C/1) and EMBO (ASTF9977) fellowships (C.A.), and Cancer Research UK and Rockefeller University (P.N.). In memoriam Heidi Browning.

Supporting Online Material

www.sciencemag.org/cgi/content/full/309/5732/297/DC1
Materials and Methods
Figs. S1 to S3
Table S1
Movies S1 to S8

12 April 2005; accepted 16 May 2005
10.1126/science.1113465

A Self-Organized Vortex Array of Hydrodynamically Entrained Sperm Cells

Ingmar H. Riedel,[1]* Karsten Kruse,[2] Jonathon Howard[1]*

Many patterns in biological systems depend on the exchange of chemical signals between cells. We report a spatiotemporal pattern mediated by hydrodynamic interactions. At planar surfaces, spermatozoa self-organized into dynamic vortices resembling quantized rotating waves. These vortices formed an array with local hexagonal order. Introducing an order parameter that quantifies cooperativity, we found that the array appeared only above a critical sperm density. Using a model, we estimated the hydrodynamic interaction force between spermatozoa to be ~0.03 piconewtons. Thus, large-scale coordination of cells can be regulated hydrodynamically, and chemical signals are not required.

Eukaryotic cilia and flagella are rodlike appendages that contain a conserved motile structure called the axoneme (*1*), an example of which is the tail of many animal spermatozoa. Oscillatory waves generated by the sperm tail propel spermatozoa through fluid, usually along helical paths. If spermatozoa approach planar surfaces, they become trapped at these surfaces and follow circular swimming paths with a strongly preferred handedness (*2*) (movie S1).

We found that the spermatozoa of sea urchins (*Strongylocentrotus droebachiensis* and *S. purpuratus*) self-organize at high surface densities into an array of vortices (Fig. 1, A and B, and movies S2 and S3) (*3*). At a density of 6000 cells/mm^2, each vortex contained 10 ± 2 spermatozoa (mean ± SD) circling clockwise (observed from inside the water phase) around a common center (Fig. 1, C to F). The circular paths had a radius of R =

13.2 ± 2.8 μm, the time for one revolution was T = 0.67 ± 0.09 s, and the swimming speed was v = 125 ± 21 μm/s. The beat frequency was f = 41.7 ± 3.7 Hz. Occasionally the hopping of spermatozoa between vortices and the fusion of two vortices were observed. The vortices were densely packed and their centers moved randomly with an apparent diffusion coefficient of D = 6.2 ± 0.9 μm²/s. This apparent diffusion coefficient is much larger than the thermal diffusion coefficient D = 0.06 μm²/s of a disk similar in size to a vortex [$D = kT/\gamma$; $\gamma = (32/3) \times \eta R$ = 0.07 μN·s/m, where radius R = 13 μm and friction in water η = 1 mPa·s] (*4*). This indicates that the array is out of thermal equilibrium because of the active propulsion of the spermatozoa (*5*, *6*), and hence the pattern is an example of self-organization (*7*–*9*). Slight changes of the microscopic parameters of such self-organized systems can lead to sudden changes in the overall pattern, making these systems amenable for regulation (*10*). We therefore analyzed the unexpected vortex array of spermatozoa to understand its underlying physical cause and to determine its possible relevance for related biological processes.

The vortex array reflected two levels of order: a clustering of spermatozoa into vortices and a packing of these vortices into an array. We assessed the packing order of the vortex array by measuring various correlation functions of the vortex centers. The pair-correlation function and the triplet-distribution function (*11*) revealed a local hexagonal order with an average vortex spacing of 49 ± 9 μm (Fig. 2). Furthermore, the bond-angular correlation function (*12*) showed an exponential decay indicating the absence of long-range order. Thus, the array is liquidlike rather than hexatic or crystalline (*12*).

We asked how the spermatozoa within a vortex influence each other (Fig. 3A and movie S4). Interactions could lead to changes in the circling radius, the swimming velocity, or the beat frequency. However, within experimental errors, we found no differences in these parameters whether spermatozoa were in a vortex or isolated. Instead, we did find a particular form of synchronization of the beating patterns of spermatozoa within a vortex: We described each spermatozoon by two variables: (i) the phase of the oscillation of the head during the beat of the spermatozoon, $\varphi(t)$ [this oscillation is driven by and has the same frequency as the oscillation of the tail (Fig. 3B)] and (ii) the angular position of the head in its trajectory around the vortex, $\Phi(t)$ (Fig. 3C). No correlation in $\Phi(t)$ between any two spermatozoa in the same vortex was found. The same was true for $\varphi(t)$. Hence, spermatozoa within a vortex swim at different speeds and beat at different frequencies. However, there is a strong correlation between the differences $\Delta\varphi(t)$ and $\Delta\Phi(t)$ between pairs of spermatozoa in the same vortex (Fig. 3, D to E). This implies, for example, that if one spermatozoon swims twice as fast as another then it also beats at twice the frequency. Thus, locally the tails are beating in synchrony and a trailing spermatozoon follows in the wake of the leading one. Because the spermatozoa swim in closed circular paths, there must be an integral number of wavelengths along the circumference of the vortex. The slope, $\Delta\varphi/\Delta\Phi$, was 4.2 ± 0.2 (Fig. 3E), consistent with a wave number of 4, which is determined by the geometry of the vortex: Dividing the circumference of the swimming path ($2\pi R$, R = 11.6 ± 3.0 μm for this particular vortex) by the beat wavelength on the sperm tail (λ = 17.6 ± 1.3 μm; along the curved centerline of the flagellar waveform, not along the arc length of the tail) gives 4.1 ± 1.4. Thus, hydrodynamic coupling of the sperm tails within a vortex leads to a quantized rotating wave with wave number 4 (Fig. 3F). This rotating wave is a generalization of the synchronization of the beats of spermatozoa swimming close to one another (*13*–*15*). Furthermore, it is related to the three-dimensional (3D) metachronal waves observed on the surfaces of ciliates and ciliated epithelia, which are important for swimming motility and the movement of mucus, where hydrodynamic interactions are also thought to play an important role (*16*, *17*).

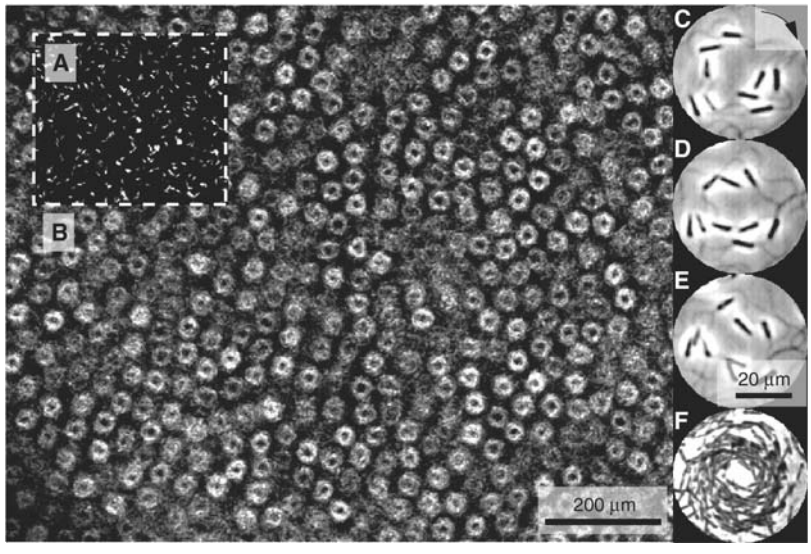

Fig. 1. Circulating spermatozoa form a 2D array of vortices. (**A**) Dark field-contrast image (single frame) showing the heads of sea urchin spermatozoa (*S. droebachiensis*) at a surface density of 6000 cells/mm². (**B**) The average intensity of 25 consecutive frames shows an arrangement of rings, each corresponding to a vortex of ~10 spermatozoa. (**C** to **E**) Successive frames of a phase-contrast movie showing nine spermatozoa swimming clockwise (arrow) within a vortex. (**F**) Average of 25 frames similar to (C) to (E) giving a magnified view of the vortices shown in (B). Frame rate, 17 frames per second (fps).

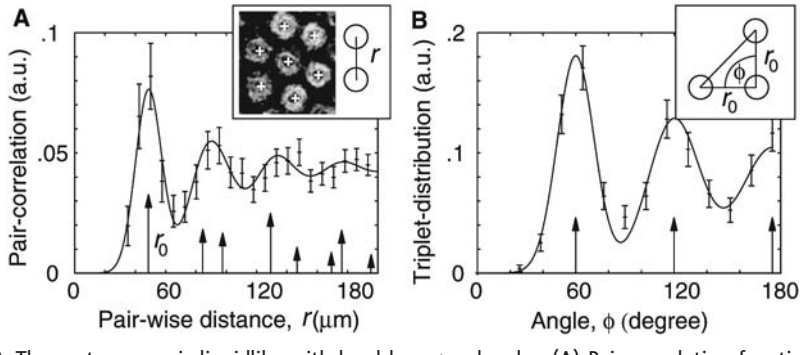

Fig. 2. The vortex array is liquidlike with local hexagonal order. (**A**) Pair-correlation function and (**B**) triplet-distribution function of the vortex centers. Insets illustrate how these functions were calculated. Arrows denote position and relative weight of the maxima for an ideal hexagonal lattice. Solid fit-lines were obtained by convoluting these maxima with Gaussians whose standard deviations increase linearly from the origin. Error bars show mean ± SEM. a.u., arbitrary units.

[1]Max Planck Institute of Molecular Cell Biology and Genetics, Pfotenhauerstrasse 108, D-01307 Dresden, Germany. [2]Max Planck Institute for the Physics of Complex Systems, Nöthnitzer Strasse 38, D-01187 Dresden, Germany.

*To whom correspondence should be addressed. E-mail: riedel@mpi-cbg.de (I.H.R.); howard@mpi-cbg.de (J.H.)

How is the vortex array formed? Because we did not observe vortex arrays at low sperm surface densities, we suspected that density might play a role in the self-organization process. To quantify the order at the different densities, we defined an order parameter χ as follows. The binary images of each movie showing only sperm heads were summed such that each pixel value in the resulting image was proportional to the number of different spermatozoa that swam over that pixel (Fig. 4A) (*3*). If the swimming paths of different spermatozoa were uncorrelated, then these pixel values would be binomially distributed. However, if spermatozoa accumulated in a vortex they would trail each other and the distribution would differ from a binomial one because low and high pixel values (corresponding to centers of the vortices and swimming trails, respectively) would be overrepresented (Fig. 4B). In this case, the variance of the measured distribution (σ_m^2) will be larger than that of the binomial distribution (σ_b^2). This motivated our definition of the order parameter $\chi = (\sigma_m^2/\sigma_b^2) - 1$, which had the expected properties: zero for a random configuration, and greater than zero if spermatozoa shared similar swimming paths. The value of χ depended on the average number of spermatozoa per vortex and how well the centers of their circular swimming paths colocalized. χ was a robust measure for the correlation among the objects and was related to the pair-correlation function [supporting online material (SOM) text]. Furthermore, χ required no labor-intensive object tracking, and hence it might be useful for quantifying order in other spatiotemporal patterns involving tracks of multiple particles or signals such as intracellular organelle transport (*18*) or ant trails (*19*).

We measured the order parameter χ for various sperm surface densities (Fig. 4C) and found a rapid change in the slope of the curve at ~2500 cells/mm^2 (fitting a Hill equation revealed a cooperativity factor of 5). This suggested a bifurcation separating a disordered and an ordered regime: one where the swimming paths of the spermatozoa were random and one where the correlation among the swimming paths increased, reflecting an increasingly pronounced vortex array.

To support this interpretation and to gain insight into the physical mechanisms underlying the pattern formation, we propose a simplified model. Each spermatozoon is represented by a point particle located at the

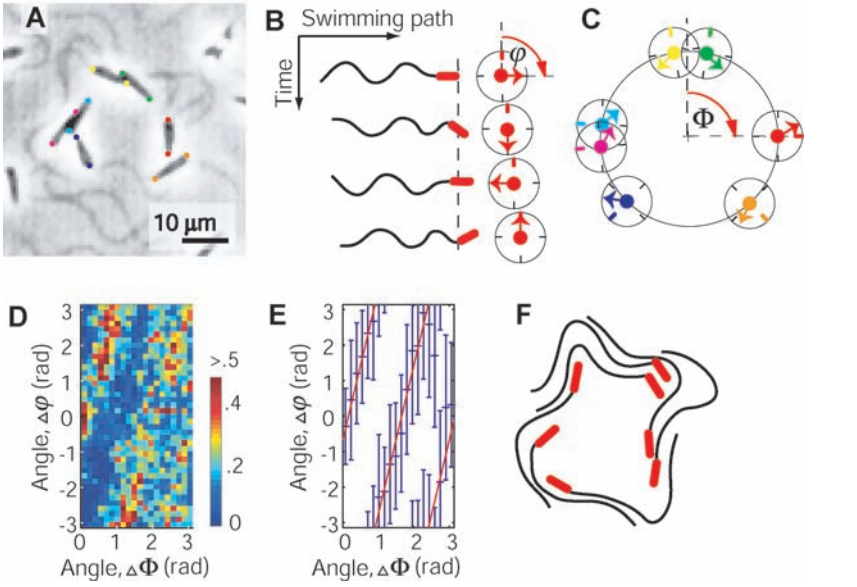

Fig. 3. Hydrodynamic coupling among spermatozoa within a vortex leads to quantized rotating waves. (**A**) Position and orientation of seven sperm heads (colored dots) within a vortex were traced. Frame rate, 250 fps. (**B**) The phases of the head oscillation were represented with circling pointers (arrow of clock, φ). (**C**) Angular positions of sperm heads within the vortex were projected onto a unit circle (center of clock, Φ; the reference frame for φ changes with Φ) (*3*). (**D**) Histogram of phase differences $\Delta\varphi$ versus $\Delta\Phi$ among any pair of spermatozoa over the observation time (color coding shows relative frequency). (**E**) In each $\Delta\Phi$ channel (D), the circular mean was obtained (errors contain 95% of the density). Linear fit (red line) $\Delta\varphi = (4.2 \pm 0.2) \times \Delta\Phi + (-0.7 \pm 0.4)$ corresponds to a quantized wave with wave number 4 (errors denote 68% confidence in fit parameters). (**F**) Illustration of the dynamics. While the spermatozoa swim around the vortex, their heads and tails oscillate. These oscillations couple hydrodynamically and form a quantized rotating wave [similar to (A)].

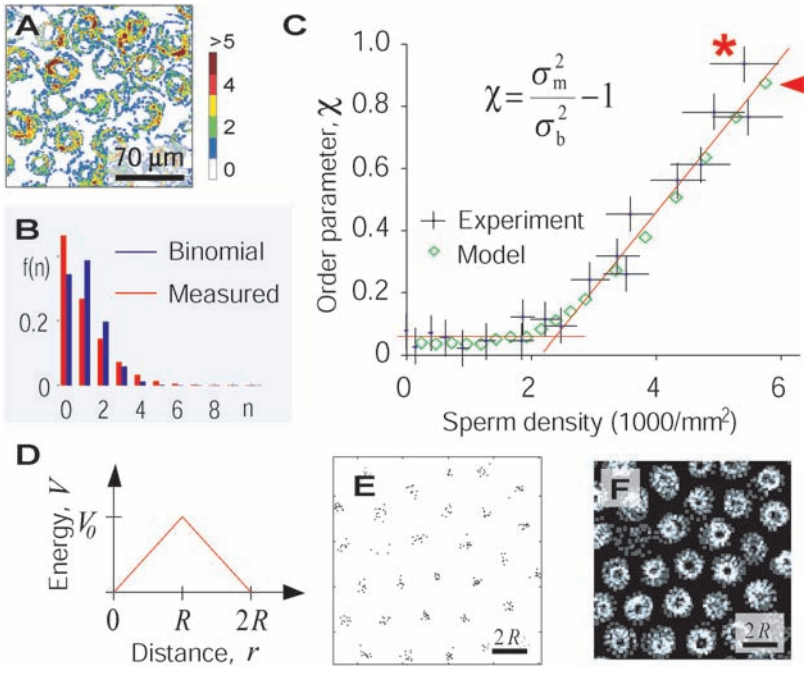

Fig. 4. The vortex array formation depends on a critical sperm density as supported by a model. (**A**) Summed-up images of a binary movie showing only sperm heads used for the calculation of the order parameter χ (*3*). Colors correspond to the number of spermatozoa that were swimming over each pixel. Frame rate, 17 fps. (**B**) Example of the expected binomial distribution (blue) versus the measured distribution (red) in (A) from which the variances σ_b^2 and σ_m^2 were obtained. (**C**) Dependence of χ on the density of spermatozoa (black crosses). The transition occurs at a sperm density of about ~2500 spermatozoa per mm^2 (red lines were inserted for visual guidance). χ obtained with the model is given as green diamonds. Asterisk and arrowhead denote data presented in (A) and (B) and in (E) and (F), respectively. Error bars show mean ± SD. (**D**) Sketch of the radial pair-interaction potential *V* used in the model with its repulsive and attractive components. *R* is the circling radius of the spermatozoon. (**E**) Result of a simulation with point particles (*3*). The hexagonal arrangement of clusters containing about 10 particles is apparent. (**F**) Average of a simulated movie generated from (E). It resembles Fig. 1B.

center of its circular swimming path. These particles move randomly with an apparent diffusion coefficient of $D = 9.0 \pm 2.0\ \mu m^2/s$, measured for isolated spermatozoa. A short-range pairwise attraction, arising from the hydrodynamic forces leading to the observed synchronization (*20*), and a longer range repulsion, which could be of steric or hydrodynamic origin (*21*), are assumed (Fig. 4D). Although one cannot describe circular flow by a potential (*22*), the important features of the observed pattern are captured by our model.

Stochastic simulations of this model (SOM text) also revealed two regimes: a random distribution of particles at low densities with a transition toward a hexagonal array of clusters at a critical particle density (Fig. 4E). Assigning to each particle a spermatozoon circling around that position, we generated simulated movies (*3*) mimicking the experimental observation (Fig. 4F versus Fig. 1B). Moreover, the order parameter χ computed for different simulated sperm densities agreed with the experimentally observed dependency (Fig. 4C). Our numerical results were further supported by a 1D mean-field analysis (SOM text), which indicated the existence of a supercritical pitchfork bifurcation at a critical sperm density (*23*). This critical density was proportional to the interaction strength and inversely proportional to the diffusion coefficient, the latter being associated with the noise in the system. This analysis demonstrates how the activity of biological processes can be regulated by critical points or bifurcations. For example, ciliary metachronal waves (*16*, *24*) might be switched on and off by small physiologically controlled changes of the activity of the individual cilia, thereby tuning the critical density for the onset of the metachronal wave.

The only free parameter in our model was the ratio of the maximum interaction potential to the drag coefficient, $V_0/\gamma = 5\ \mu m^2/s$, which was chosen to match the critical density (Fig. 4C). This allowed us to estimate the interaction force between two spermatozoa $F_{int} = |\mathrm{grad}(V)| = (V_0/\gamma) \times \gamma/R \sim 0.03$ pN (using $R = 13\ \mu m$ and $\gamma = 0.07\ \mu N \cdot s/m$ from above). This force is about 1% of the forward propulsion force of spermatozoa $F_{for} \sim 5$ pN (*25*). Although this hydrodynamic interaction force is smaller than typical adhesion forces involved in sperm cooperation (*26*), it is evidently large enough to coordinate the cells and to regulate large-scale pattern formation in the absence of chemical signals (*27*).

References and Notes

1. I. R. Gibbons, *J. Cell Biol.* **91**, 107s (1981).
2. D. M. Woolley, *Reproduction* **126**, 259 (2003).
3. Materials and methods are available as supporting material on *Science* Online.
4. H. C. Berg, *Random Walks in Biology* (Princeton Univ. Press, Princeton, NJ, 1993).
5. X. L. Wu, A. Libchaber, *Phys. Rev. Lett.* **84**, 3017 (2000).
6. N. Darnton, L. Turner, K. Breuer, H. C. Berg, *Biophys. J.* **86**, 1863 (2004).
7. A. M. Turing, *Philos. Trans. R. Soc. London Ser. B* **237**, 37 (1952).
8. I. Prigogine, G. Nicolis, *J. Chem. Phys.* **46**, 3542 (1967).
9. T. Misteli, *J. Cell Biol.* **155**, 181 (2001).
10. F. J. Nédélec, T. Surrey, A. C. Maggs, S. Leibler, *Nature* **389**, 305 (1997).
11. K. Zahn, G. Maret, C. Russ, H. H. von Grünberg, *Phys. Rev. Lett.* **91**, 115502 (2003).
12. K. Zahn, R. Lenke, G. Maret, *Phys. Rev. Lett.* **82**, 2721 (1999).
13. J. Gray, *Ciliary Movement* (Cambridge Univ. Press, New York, 1928).
14. J. Gray, G. J. Hancock, *J. Exp. Biol.* **32**, 802 (1955).
15. G. I. Taylor, *Proc. R. Soc. London Ser. A* **209**, 447 (1951).
16. K. I. Okamoto, Y. Nakaoka, *J. Exp. Biol.* **192**, 61 (1994).
17. S. Gueron, K. Levit-Gurevich, *Biophys. J.* **74**, 1658 (1998).
18. E. Nielsen, F. Severin, J. M. Backer, A. A. Hyman, M. Zerial, *Nat. Cell Biol.* **1**, 376 (1999).
19. B. Hoelldobler, E. O. Wilson, *The Ants* (Springer, Berlin, 1990).
20. L. J. Fauci, A. McDonald, *Bull. Math. Biol.* **57**, 679 (1995).
21. P. Lenz, J. F. Joanny, F. Jülicher, J. Prost, *Phys. Rev. Lett.* **91**, 108104 (2003).
22. L. D. Landau, E. M. Lifshitz, *Fluid Mechanics, Course of Theoretical Physics* (Pergamon Press, Oxford, 1987).
23. S. H. Strogatz, *Nonlinear Dynamics and Chaos* (Westview Press, Cambridge, MA, 2000).
24. M. A. Sleigh, Ed., *Cilia and Flagella* (Academic Press, London, 1974).
25. J. Howard, *Mechanics of Motor Proteins and the Cytoskeleton* (Sinauer Associates, Sunderland, MA, 2001).
26. H. Moore, K. Dvorakova, N. Jenkins, W. Breed, *Nature* **418**, 174 (2002).
27. C. Dombrowski, L. Cisneros, S. Chatkaew, R. E. Goldstein, J. O. Kessler, *Phys. Rev. Lett.* **93**, 098103 (2004).

28. We thank D. Babcock, C. Brokaw, R. Goldstein, F. Jülicher, H. Machemer, K. Müller, F. Nédélec, E. Schäffer, and members of the Howard lab and Jülicher lab for discussions and comments on the manuscript. All authors contributed ideas and discussion, and I.H.R. carried out experiments, programming, and data analysis.

Supporting Online Material

www.sciencemag.org/cgi/content/full/309/5732/300/DC1
Materials and Methods
SOM Text
Figs. S1 to S6
References
Movies S1 to S5

27 January 2005; accepted 24 May 2005
10.1126/science.1110329

Inferential Structure Determination

Wolfgang Rieping,* Michael Habeck,* Michael Nilges†

Macromolecular structures calculated from nuclear magnetic resonance data are not fully determined by experimental data but depend on subjective choices in data treatment and parameter settings. This makes it difficult to objectively judge the precision of the structures. We used Bayesian inference to derive a probability distribution that represents the unknown structure and its precision. This probability distribution also determines additional unknowns, such as theory parameters, that previously had to be chosen empirically. We implemented this approach by using Markov chain Monte Carlo techniques. Our method provides an objective figure of merit and improves structural quality.

A major difficulty in the determination of three-dimensional macromolecular structures is that experimental data are indirect. We observe physical effects that depend on the atomic geometry and use a forward model to relate the observed data to the atomic coordinates. For example in nuclear magnetic resonance (NMR), the intensity I_i of peaks in nuclear Overhauser effect spectroscopy (NOESY) data is proportional to the inverse sixth power of the distance d_i of two spins: $I_i = \gamma d_i^{-6}$ (*1*). This isolated spin pair approximation (ISPA) involves an unknown scaling factor γ. It seems straightforward to obtain the structure in the example: simply use the observed intensities to calculate sufficient distances to define the structure.

In realistic applications, this approach runs into difficulties. One problem is that the forward model is usually inherently degenerate, meaning that different conformations can lead to the same observations and therefore cannot be distinguished experimentally, and even a formally invertable forward model is practically degenerate if the data are incomplete. A further complication is that there are uncertainties in both the data and the forward model: Data are subject to experimental errors, and theories rest on approximations. Moreover, the forward model typically involves parameters that are not measurable. Algorithms for structure calculation from x-ray reflections, NMR spectra, or homology-derived restraints should account for these fundamental difficulties in some way.

Structure determination in general is an ill-posed inverse problem, meaning that going from the data to a unique structure is impossible. However, the current paradigm in structure calculation is to attempt an inversion of the forward model. Most algorithms minimize a hybrid energy $E_{hybrid} = E_{phys} +$

Unité de Bioinformatique Structurale, Institut Pasteur, CNRS URA 2185, 25-28 rue du Docteur Roux, 75724 Paris CEDEX 15, France.

*These authors contributed equally to this work.
†To whom correspondence should be addressed. E-mail: nilges@pasteur.fr